SONAR

DELIVERABLE REPORT

Deliverable no. / title:	D3.7 Scaling strategies 3
Lead beneficiary:	CNRS-LRCS
Nature of deliverable:	Report
Dissemination level:	PU– Public
Due date:	M45 / September 2023
Grant Agreement number:	875489
Project acronym:	SONAR
Project title:	Modelling for the search for new active materials for redox flow batteries
Funding scheme:	H2020-LC-BAT-2019
Coordinator:	Fraunhofer ICT Jens Noack **Tel:** 0049 721 4640 870 **E-mail:** jens.noack@ict.fraunhofer.de
Project website:	www.sonar-redox.eu

Table of contents

1 Introduction

This report reformulate the contents published in the paper [Yu, J., Duquesnoy, M., Liu, C., Franco, A.A. (2023), **Optimization of the microstructure of carbon felt electrodes by applying the lattice Boltzmann method and Bayesian optimizer**, Journal of Power Sources, Volume 575, 233182, ISSN 0378-7753.](#)

In the previous delieverable reports, we have presented our kinetic Monte Carlo models which focus on the explicit molecular level. Among the three mass transfer phenomena, only diffusion and migration were taken into account. However, convection also plays a vital role in the RFB systems, as the electrolyte flow is constantly pumping through the reaction chamber. Therefore, the original goal of this delievrable is to simulate the electrolyte flow inside RFBs and upscale the model.

However, alongside the model development, we notice that the arrangement of fibres, the porosity, and the compression ratio of the carbon felt electrode impact significantly on the fluid dynamics of the electrolyte flow. Consequently, we end up proposing a complete computational methodology to optimise the microstructure of the carbon felt electrode employed in RFBs within this deliverable report.

Drawing upon our practical knowledge, it is evident that poor circulation of the electrolyte flow decreases the system efficiency (Figure 1). As such, we fix our optimisation objective to quantitatively maximise the electrolyte utilisation rate. This maximisation depends on three aspects: the specific surface area, the hydraulic permeability, and the practical reactive volume. We introduce the concept of a practical reactive volume to quantify the dead zone where the electrolyte flow is too slow to react, thereby leading to the waste of the active surface area.
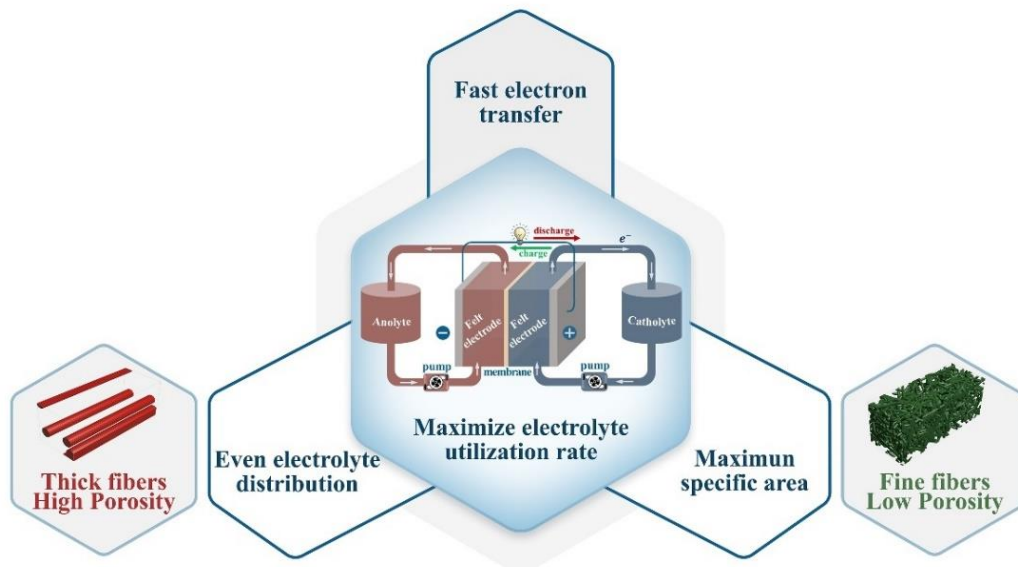
Figure 1. Schematic showing the three factors required to maximize the electrolyte utilization rate in an RFB system.

By synergistically combining stochastic generation of the electrode microstructure, digital compression of the electrode, the Lattice Boltzmann Method, and the Bayesian optimisation approach, we establish our computational workflow to predict an optimised set of parameters for electrode design. The optimisation algorithm evaluates three microstructure properties at each cycle and proposes a new combination of parameters for examination in the next cycle. Throughout this workflow, we have tested a total of 240 parameter sets using the Bayesian Optimiser.

The optimisation results demonstrate that a high compression ratio with thick, aligned fibres favours enhanced electrode performance. In the case of a highly compressed felt electrode, the pore size generally decreases while a small number of large-sized pores persist in the structure, thereby facilitating convection in the electrolyte flow. Contrary to conventional thought, which suggests that fine fibres with low porosity yield a larger specific surface area, our simulations reveal that thick, aligned fibres with a high compression ratio provide a superior balance between hydraulic permeability, specific surface area, and practical reactive volume.

Considering the heavy computational cost of coupling the lattice Boltzmann model with the kinetic Monte Carlo model, the properties obtained from our optimised structure and an unfavourable structure are incorporated into a homogeneous model to simulate electrochemical performance

during charge and discharge. In this simulation, the optimised case demonstrates a lower overpotential and a better reversible capacity compared to the non-optimised one.

2   Workflow and modelling methodology

2.1   Optimization target parameters

We target a combination of related parameters to be optimized, including the fibre diameter, the density of the felt, fibre orientation, amount of in-plane fibre, and compression ratio of the felt electrode. The range of each parameter is listed in Table 1.

Table 1. Parameter range of the optimization workflow

Parameter	Min value	Max value
Fiber diameter (μm)	4.70	22.3
Density (g cm^{-3})	0.08	0.15
Fiber orientation	1.0	9.0
Amount of through-plane fibre (%)	0.5	10
Compression ratio (%)	1.0	40.0

Considering the usage in industrial manufacturing, we choose bulk density instead of porosity in our study as one of the optimization parameters. The respective porosity ranges from 0.89 to 0.94 without compression. The value of fibre orientation controls the stochasticity of the fibre. The fibre is perfectly aligned in the direction of the electrolyte flow (x-axis) with a value of 10 and the orientation of the fibre is randomly assigned the value of 0. To respect the manufacturing process of the felt electrode, the value of the fibre orientation is chosen to be in the range from 1 to 9 to control the randomness of the fibre orientation. Furthermore, since a small amount of through-plane fibre is required for fabricating the stitched felt electrode, a certain amount of through-plane fibre, from 0.5% to 10%, is also considered. The orientation of the through-plane fibres is restricted to the z-axis direction with limited stochasticity. The compression considered in this study is the path-controlled surface pressure along the z-axis. According to Banerjee et al., the permeability of the felt electrode decreases sharply after a 40% compression. Thus, we set 40% as the maximum compression ratio. [1]

SONAR Deliverable Report

2.2 The optimization workflow and the microstructure generation

The schematic of the optimization workflow used in this study is shown in **Figure 1**. For each set of parameters, the electrode is first generated and compressed in GeoDict® based on the related parameter set. Since the compression can change the size of the electrode, the optimization workflow is made consistent by setting the initial volume of the electrode to $1000 \times 220 \times 350 \ \mu m^3$, and cutting into the same volume of $1000 \times 200 \times 200 \ \mu m^3$ after the compression. Then, we obtain our first optimization property from the compressed microstructure, *i.e.*, the specific surface area, *SSA*.

In this study, the *SSA* is estimated according to the determination of the four Minkowski measures, *i.e.*, volume, surface area, integral of the mean curvature, integral of total curvature, from the voxelized images in the MatDict module of GeoDict® [2,3]. Compared to the *SSA* calculated based on the voxel mesh, the Minkowski measurement is more accurate and realistic due to the reconstruction of the actual geometry.

The obtained microstructure is then injected into the LBM model to calculate the fluid velocity distribution and the hydraulic permeability, *k*. The last optimization property, the practical reactive volume, is calculated based on the post-analysis of the LBM results. BO takes the properties obtained from each iteration and predicts the next optimized parameter set for the following iteration.
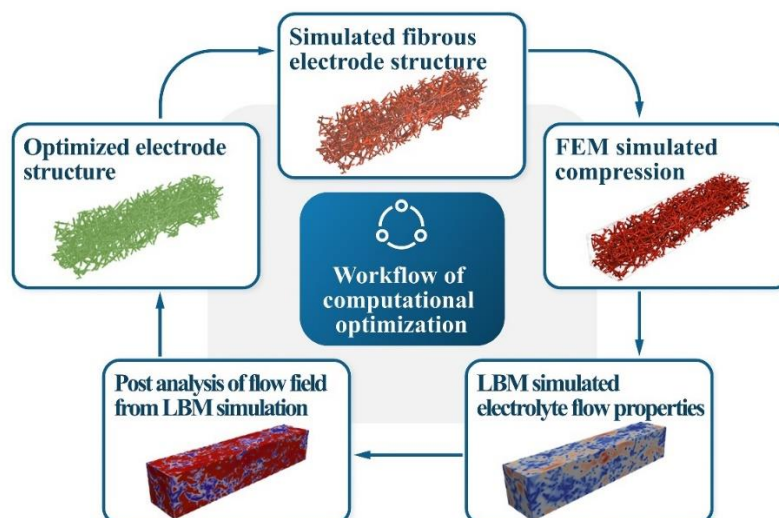

Figure 1. Schematic for the computational workflow for the optimization of the carbon felt electrode microstructure.

2.3 The LBM model

The approach utilized in this delieverable report follows the well-established LBM. Within this LBM framework, the intricate interplay between electrolyte and electrode microstructures finds representation upon a cubic lattice. The fluid dynamics of the electrolyte are transcribed through the displacements of discrete fluid particles, constrained to predefined directions.[4] To formulate our LBM model, we opted for a three-dimensional cubic lattice employing 19 fixed velocity vectors (D3Q19), coupled with the venerable Bahtnagar-Gross-Krook (BGK) collision operator.

According to the general idea of LBM, the displacement of each electrolyte particle can be described as follows,

$$f_i(x + e_i\delta t, t + \delta t) - f_i(x,t) = \Omega_i + F_b, \qquad i = 0,1,2,\dots,18 \tag{1}$$

where f_i is the particle distribution function, and e_i is the particle velocity at lattice location x at time t. The subscript i represents the velocity vector i around the grid unit, with 19 directions in our LBM approach. Ω_i is the collision operator at lattice node x at time t, which together with the particle distribution function, f_i, holds the system in Maxwellian equilibrium.

In the present work, a classic Bahtnagar-Gross-Krook (BGK) operator is chosen due to its simplicity and the low speed of electrolyte flow inside RFB system, which is expressed as:

$$\Omega_i^{BGK} = \frac{-1}{\tau}\left[f_i(x,t) - f_i^{eq}(x,t)\right], \tag{2}$$

where τ is the relaxation time related to the kinematic viscosity of the electrolyte v, which is calculated through $v = c_s^2\left(\tau - \frac{1}{2}\right)$.[5] c_s is the lattice speed sound defined by $c_s = \frac{\frac{\delta t}{\delta x}}{\sqrt{3}}$, where δt and δx are the discrete-time step and length step, respectively.

The $f_i^{(eq)}$ is the particle distribution function at the equilibrium state, which can be obtained through,

$$f_i^{(eq)}(x,t) = \omega_i\rho\left(1 + \frac{e_i \cdot U}{c_s^2} + \frac{(e_i \cdot U)^2}{2c_s^4} - \frac{U^2}{2c_s^2}\right), \tag{3}$$

where ω_i is the weighting factor for velocity vector i, where $w_i = \frac{1}{3}$ for $i = 0$, $w_i = \frac{1}{18}$ for $i = 1, \dots, 6$ and $w_i = 1/36$ for $i = 7, \dots, 18$. ρ is the density of the fluid. U is the dynamic fluid velocity. e_i is the discrete velocity defined as,

$$[e_0, e_1, e_2, e_3, e_4, e_5, e_6, e_7, e_8, e_9, e_{10}, e_{11}, e_{12}, e_{13}, e_{14}, e_{15}, e_{16}, e_{17}, e_{18}] = c$$

$$\begin{bmatrix} 0 & 1 & -1 & 0 & 0 & 0 & 0 & 1 & -1 & -1 & 1 & -1 & 1 & 1 & -1 & 0 & 0 & 0 & 0 \\ 0 & 0 & 0 & 1 & -1 & 0 & 0 & -1 & 1 & -1 & 1 & 0 & 0 & 0 & 0 & 1 & -1 & 1 & -1 \\ 0 & 0 & 0 & 0 & 0 & 1 & -1 & 0 & 0 & 0 & 0 & 1 & 1 & -1 & -1 & -1 & 1 & 1 & -1 \end{bmatrix} \tag{4}$$

SONAR Deliverable Report

The density and velocity of the fluid are obtained from the following discrete distribution functions:

$$\rho(x,t) = \sum_{i=0}^{n} f_i(x,t) \tag{5}$$

$$\rho(x,t)U(x,t) = \sum_{i=0}^{n} e_i f_i(x,t). \tag{6}$$

The system is exposed to a constant pressure difference, P, between the inlet (x = 0) and the outlet (x = 1000) in our LBM model. The pressure difference is implemented as an external force, F_b, whose impact is added to the velocity of the fluid as:

$$U^{eq}(x,t) = U(x,t) + \frac{\tau F_b}{\rho}. \tag{7}$$

We assume the carbon felt electrode is filled with electrolyte with a velocity of 0 at the beginning of the LBM simulation. The velocity distribution of the electrolyte flow reached a steady state under the constant pressure difference along the x-axis direction. The hydraulic permeability, k, is calculated from $k = \frac{\mu \bar{U}}{P}$, based on the results obtained from the LBM model, where $\bar{U}$ is the averaged flow fluid velocity, and μ is the dynamic viscosity of the electrolyte.

As demonstrated by Kok et al., a significant portion of the reactive surface might be starved from the reactant due to the heterogeneity of the fibrous electrode.[6] Therefore, we introduce another property, *i.e.*, the practical reactive volume, aside from the specific surface area and hydraulic permeability, to better evaluate the mass transport in the system. The practical reactive volume is estimated based on the Peclet number. The Peclet number is calculated for each mesh unit through the characteristic length, L, the velocity distribution obtained from LBM, U_i, and the diffusion coefficient for the chosen species, D, as shown in Eq. 5.9.

$$Pe = \frac{LU_i}{D} \tag{9}$$

In this study, we chose $D = 5.5 \times 10^{-6}$ cm^2·s^{-1}.[7] Convection is considered not to hinder the diffusion of the active species once $Pe \gg 1$.[8] Therefore, we set the threshold of $Pe = 100$. For each mesh unit, the convection is considered not enough if the Peclet number is lower than 100. The practical reactive volume is then calculated through the ratio between the sum of unit volume where $Pe \geq 100$ and the total reactive volume (without solid fiber), as shown:

$$\eta_{PRV} = \frac{V_{Pe \geq 100}}{V_{tot}} \tag{10}$$

SONAR Deliverable Report

The LBM model is coded in C++ based on the Palabos package [9,10] and previous work by Santos *et al.*[11] The post-processing of the resulting data was carried out in Paraview [12] and Python3.7 [13].

2.4   Bayesian optimizer (BO)

BO was applied to optimize the specific surface area, hydraulic permeability, and practical reactive volume simultaneously. BO combines these properties to reflect a multi-objective optimization problem through an objective function (denoted C_f) to be minimized:

$$C_f = min\left(\frac{1}{3}(1 - SSA)^2 + \frac{1}{3}(1 - k) + \frac{1}{3}(1 - \eta_{PRV})\right) \tag{11}$$

Such a function is dependent on the input parameters and needs to be approximated by the BO framework to target the most suitable candidate of parameters to minimize C_f. We assign the same weight for each property to balance their importance in the optimizer. In each iteration of the BO algorithm, a posterior distribution $C_f|D$ is calculated by probabilistic modelling, where D is the set of previous data that have been proposed. Then the algorithm proposes a new candidate of input parameters chosen by an acquisition function. Such a function balances the exploration of identifying value combinations far from prior parameters and the exploitation of prior parameter combinations to pinpoint nearby the minima. In our study, we used a Gaussian process regression to approximate C_f, updated at each iteration to return the best combination of input parameters providing a good balance between the optimal properties.

As we intend to maximize the specific surface area, hydraulic permeability, and practical reactive volume, we built the objective function C_f with the following purposes:

a)   Proper weights given for each property.

b)   Tackle the different orders of magnitude.

To do so, we evaluated a scalarization method over C_f by incorporating a scalar fitness function, allowing each property tobe fit into [0, 1] for the evaluation of the C_f. More precisely, this strategy addresses any bias that could appear when maximizing all three properties regarding the existing relationships. Each scaled property *X* was included in C_f as (*1-X*) to be minimized when the associated property needs to be maximized. As a consequence, C_f respects an equal-weighted power function:

$$\mathbf{X}^* = argmin_x\left(C_f(x)\right) \tag{12}$$

SONAR Deliverable Report

Regarding each iteration of the BO framework, the evaluation of C_f denotes a non-linear combination of electrode properties calculated from the previous steps, reducing the number of parameters sets to test and giving an optimal balance of the properties, as mentioned earlier.

3 Results and discussion

Our algorithm workflow tested 240 parameter sets in total. The total convergence of the workflow is plotted in Figure 1 (a). and Figure 1 (b) presents the convergence of the hydraulic permeability and the specific surface area. It is observed that the minimum value of C_f appears after 55 iterations. The *SSA* reaches the maximum after 35 iterations, and the maximum permeability is reached after 222 iterations.
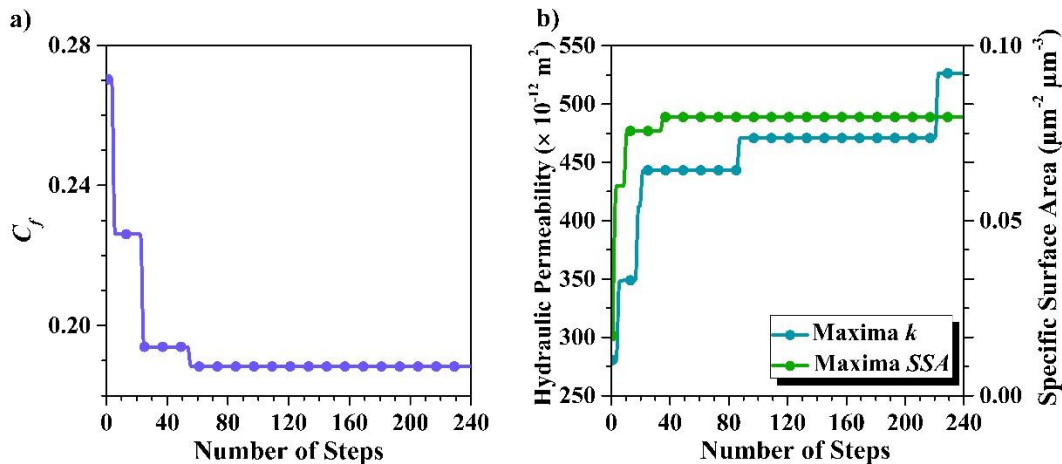

Figure 1. Convergence curve of the BO algorithm. (a) The minima of C_f after each iteration. (b) The maxima of the hydraulic permeability and the SSA after each iteration.

The distribution of each property obtained from our workflow is presented in Figure 2 (a), (b), and (c). Each data point represents an obtained value from the workflow. The colour bar is assigned based on the value of the optimization function, C_f. Figure 2 (a) illustrates the decreasing correlation trend between the specific surface area and the practical reactive volume. The sharp decrease of permeability when the specific surface area increases is illustrated in Figure 2 (b). Figure 2 (c) presents the increasing correlation between the practical reactive volume and hydraulic permeability.
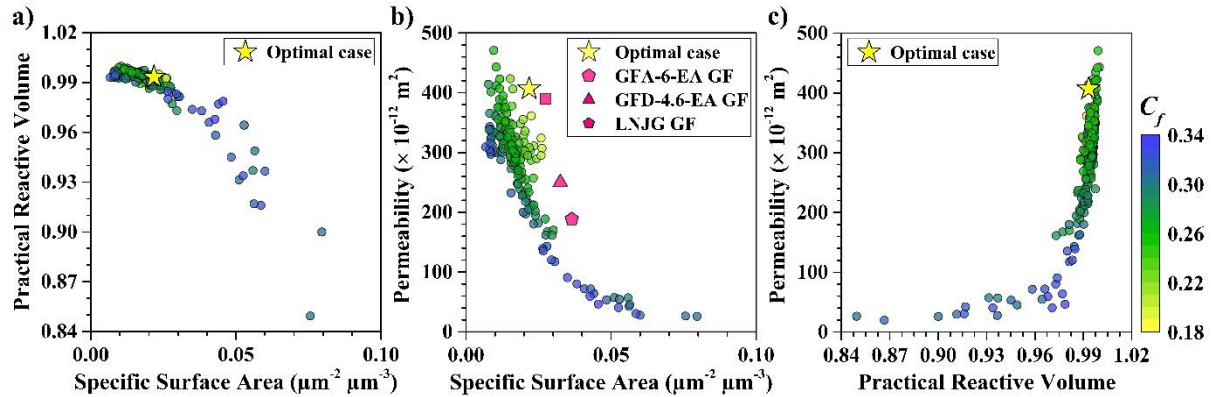
Figure 2. Distribution of the three optimization properties and the three reference cases. (a) The distribution of SSA versus PRV. (b) The distribution of SSA versus Hydraulic permeability. (c) The distribution of PRV Vs. Hydraulic permeability.

The ideal case with an optimized value of C_f in this study needs to maximize all three properties in Figure 2. As can be seen in Figure 2 (a), (b), and (c), the colour of the data points gradually becomes yellow from left to right and from bottom to up. Moreover, the predicted optimal case is located in the top half and the right-hand side of all three sub-figures. The cluster of data points in the hydraulic permeability range of $(280 - 420 \times 10^{-12}$ m$^2)$ demonstrates the functionality of the optimizer. After the appearance of the first optimized case, the optimizer starts to extrapolate the parameter sets close by to identify the next optimized parameter set.

Three reference values of *SSA* and hydraulic permeability of the commercialized graphite felt electrodes are also included in Figure 2b), which are compared with our predicted optimal case.[14] The *SSA* of the three reference cases was extracted from the tomography results by calculating the cubic voxel facets of the solid-liquid interphase. Compared to the *SSA* calculated by Minkowski measures in our approach, the obtained reference results are relatively higher than the actual value. We also estimated the apparent SSA and the SSA calculated from the sum of the voxel facets for each microstructure generated in our workflow. The apparent *SSA* is calculated through the cylinder surface area, considering that the fibrous material is one fibre only. Figure 3 compares the *SSA* obtained from the three different methods. The colour bar of the dots is assigned based on the density of the felt electrode. Figure 3 (a) presents the apparent *SSA* and the *SSA* obtained from the Minkowski measures. The apparent *SSA* is considered a reference value, and the Minkowski value demonstrates a linear correlation with the apparent *SSA*, except

SONAR Deliverable Report

for several points. The apparent *SSA* does not consider the intersection of the fibres and is calculated based on the compressed structure without the sample size unification, which could explain the appearance of the deviated points. On the other hand, The *SSA* calculated by the sum of the voxel facet presented in Figure 3 (b) demonstrates a much higher value than the apparent *SSA* for all the data points. Moreover, no clear trend between these two methods can be determined due to the multi-parameters required for the structure generation.
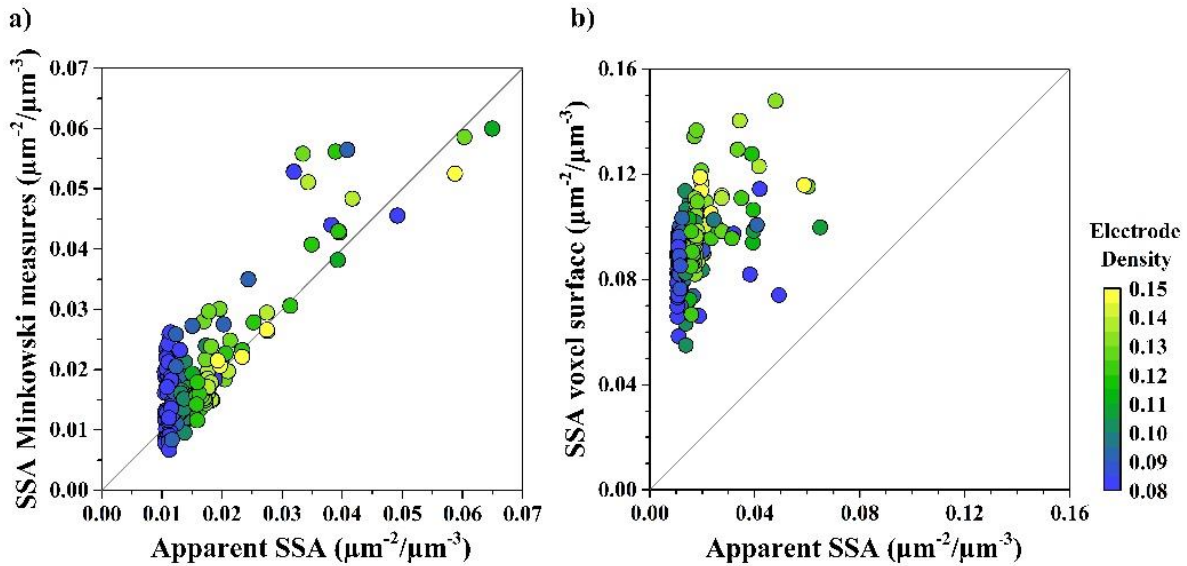

Figure 3. Comparison of SSA calculated from voxel facet surface and the Minkowski measures.

Furthermore, electrode compression, leading to decreased hydraulic permeability and increased *SSA,* is not considered for the three reference cases. Therefore, the prediction of the optimal case in our study reaches a higher permeability with a similar *SSA* for the three reference cases.

Table 1 presents the predicted parameter set of the optimal case, and the microstructure of the optimal case is shown in Figure 4. Compared to the optimization case proposed by Wan *et al.* [14], our optimal case favours a thick fibre with a high compression rate instead of a thin fibre and high porosity. However, the porosity of our optimal case is 0.91, which is in agreement with the optimized case of Wan *et al.*, which brings our attention to the impact of compression on the pore network of the electrode.
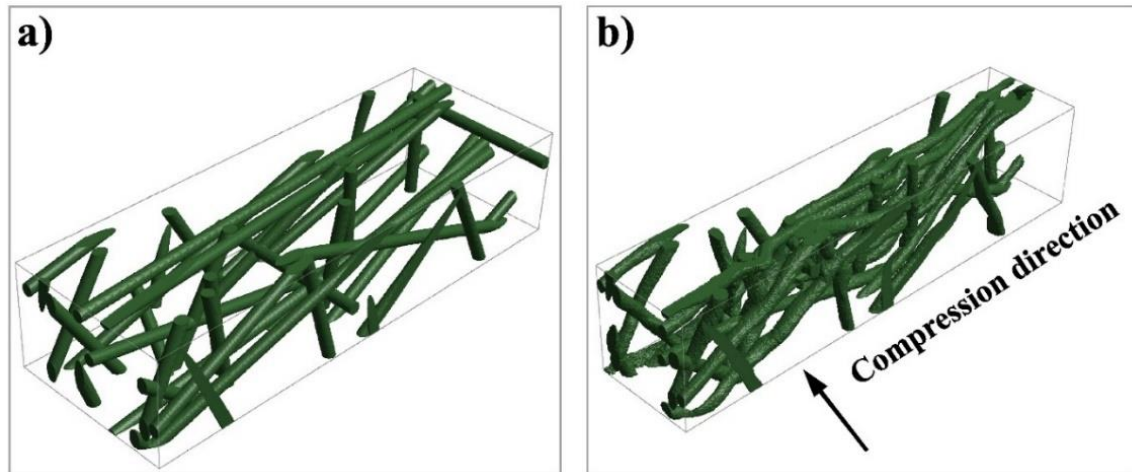
Figure 4. Electrode microstructure of the optimal case. (a) Before compression. (b) After compression.

Table 1. Parameter sets of the best case.

Parameter	Optimal case
Fiber diameter (µm)	22.3
Density (g cm^{-3})	0.08
Fiber orientation	8.55
Amount of through-plane fibre (%)	2.30
Compression ratio (%)	32.6
C_f	0.188

Figure 4 (b) shows that the electrode structure adapted in the optimization function only contains a small number of fibres and pores due to volume limitation, which is not enough for conducting a complete study of the pores. Therefore, we reconstructed a more extensive sample by taking the proposed parameter set, as shown in Figure 5 (c).

Figure 5 (a) and (b) illustrate the identification of pores by the Watershed Algorithm before and after compression. Each identified pore is illustrated in one specific colour to facilitate the

visualization. The compression decreases the pore size and increases the pore network. Figure 5 (d) presents the histogram of the pore size distribution based on the pore diameters. Compression reduces the pore size, leading to a shift of the peak to the left. Moreover, the electrode structure demonstrates a heterogeneous porosity distribution along the compression direction. (Figure 5 (e)).

The porosity of the electrode microstructure near the compressed plane decreases more than the bulk level, while the rest of the microstructure does not demonstrate a significant change above the bulk level. This heterogeneous porosity distribution facilitates the convection of the electrolyte while offering a significant number of reaction sites.[15,16] As presented in Figure 5 (d), a small fraction of the large-size pores with a diameter of around 200 μm remains in the system, facilitating the electrolyte flow's mass transport process.[16]

Figure 5 (f) presents the Krumbein sphericity of the pores before and after the compression. The Krumbein sphericity, P_k, is calculated based on the three principal axes, a, b, and c, of the ellipsoid fitted to each pore through: $P_k = \sqrt[3]{\frac{bc}{a^2}}$. The closer the value of P_k is to 1, the shape of the pore is closer to a sphere. On the other hand, the pore shape is flatter or more prolate when P_k is closer to 0. The amount of sphere-shaped pores increases after the compression, because the large pores are separated into smaller pieces after compression. Meanwhile, the amount of prolate pores also increases, as the width of the pores are generally reduced due to the compression.

Compared to the optimal case discussed previously, the microstructure of the non-ideal case is generated with thin fibre, high bulk density, and random in-plane fibre orientations. The total porosity is 0.87 after compression, which leads to weak electrolyte fluidity and low practical reactive volume.

To further validate our optimization results, an electrochemical model is built in COMSOL® to simulate the charging and discharging process of V^{3+}/ V^{2+}. In this model, a cardon felt electrode with the size of 5 cm × 5 cm × 2 mm is depicted as a homogenized 2D plane. The SSA, permeability, and porosity of the predicted optimal case and the non-ideal case are implemented in the homogeneous model and shown in Table 2. We assume the same pressure is applied to both systems. The modelling details can be found in the Supporting Information. Four current densities are applied to the electrode: 5 mA cm^{-2}, 10 mA cm^{-2}, 20 mA cm^{-2}, and 40 mA cm^{-2}.
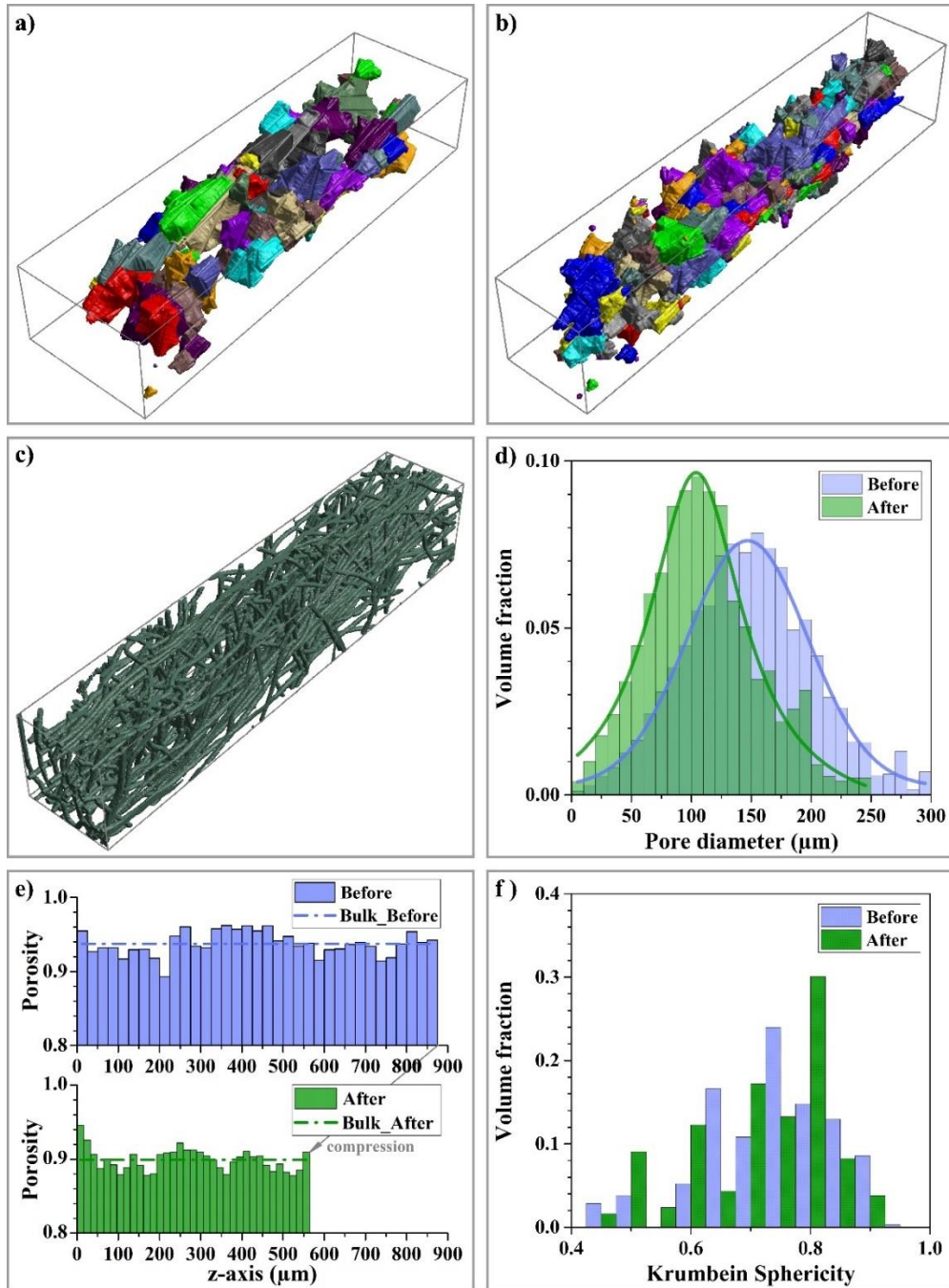
Figure 5. (a) Identification of pores before compression. (b) Identification of the pores after compression. (c) The electrode structure generated from the parameter set of the optimal case in a more significant volume (3000 × 550 × 875 μm^3). (d) Pore size distribution before and after compression. (e) Pore size distribution along the compression direction (z-axis) before and after compression. (f) Krumbein sphericity of the electrode structure before and after compression.

SONAR Deliverable Report

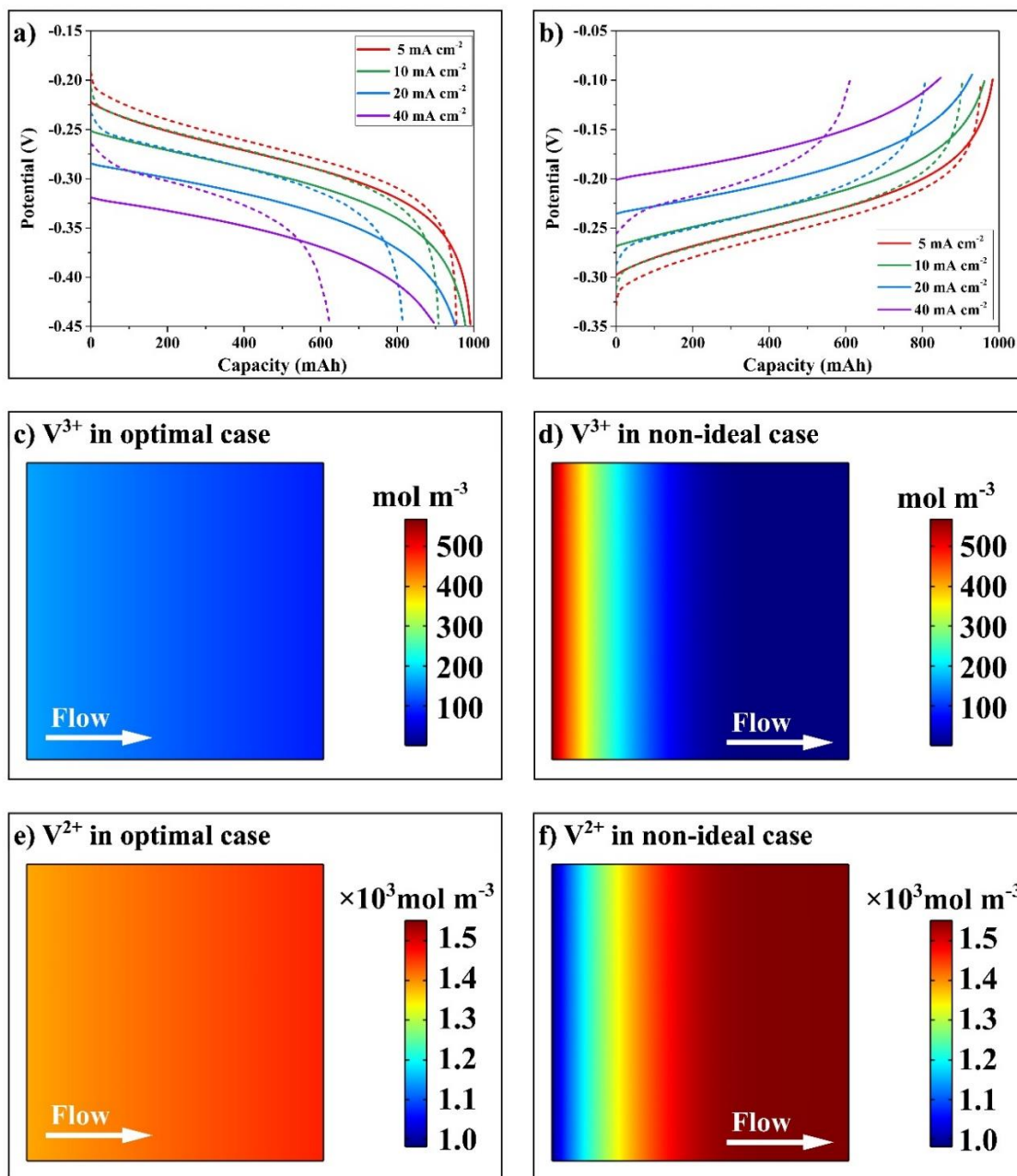**Figure 6. a) Discharge profiles of V^{3+} with different current densities. Solid lines represent the optimal electrode structure, and the dashed lines represent the non-ideal case. b) Charge profiles of V^{2+} with different current densities. Solid lines represent the optimal electrode structure, and the dashed lines represent the non-ideal case. c)- f) Concentration distribution in the electrode 2D plane.**

The obtained charge and discharge profiles are shown in Figure 8 a) and b). Results show that the optimal electrode has better performance than the non-ideal electrode in charge and discharge by showing higher reversible capacity. We notice that the two curves always intersect for each applied current density. Before the intersection, the optimal electrode always shows a higher absolute overpotential value due to the relatively low SSA, leading to a high faradaic current density on the fibrous surface. However, the curves of the optimal electrode still extend longer than the non-ideal electrode after the intersection. As the optimal electrode is equipped with thick fibre and a high compression ratio, its structure favours the electrolyte convection, leading to the better transportation of the active species. Figure 8 c), d), e), and f) show the concentration distribution of V^{2+} and V^{3+} at the end of discharging process with the current density of 40 mA cm^{-2}. As can be seen, the optimal electrode shows a much lower concentration gradient than the non-ideal electrode, implying that efficient transportation promotes a thorough electrochemical reaction.

Table 2 Characteristics of the optimal case and non-ideal case in the homogeneous model

	Optimal case	Non-ideal case
Porosity	0.91	0.87
SSA ($m^2 m^{-3}$)	21754	45545
Velocity of the flow (mm s^{-1})	1.11	0.13

4 <u>Conclusion</u>

In this , we present a computational workflow to optimize the microstructure of the carbon felt electrode. Such an optimization aims to maximize the electrolyte utilization rate by maximizing three properties, including the specific surface area, the hydraulic permeability, and the practical reactive volume. We extract the properties of electrode microstructure generated stochastically by GeoDict® and the LBM model. The latter is applied to investigate the fluid dynamic properties of electrolytes passing through felt electrodes and quantify the 'starved zone' by calculating the Peclet number. The BO predicts a newly optimized parameter set based on the optimization function of each iteration. Our approach also offers a method to investigate the mass transport phenomenon separately from the electrochemistry reactions.

This study is industry-oriented and offers some practical insights for better-felt electrode designs. The optimization algorithm results show that the felt electrode with fine fibres, high density, and

high compression ratio achieves a vast surface area, causing poor electrolyte circulation and leading to low hydraulic permeability and low practical reactive volume. On the contrary, felt electrode with thick fibres, low density, and low compression rate facilitates the convection of the electrolyte flow and decreases the specific surface area. Besides, among the five input parameters, the amount of in-plane fibre demonstrates a weak influence on the value of C_f.

The predicted optimal case is generated with thick fibre diameters, low density, aligned through-plane fibre, and a high compression rate, which reaches a higher hydraulic permeability than the commercialized reference cases and similar specific surface area. In addition, the impact of the compression on the geometrical change is thoroughly investigated. The felt electrode demonstrated heterogeneity regarding the pore size distribution along the compression direction. The huge fraction of small-sized pores offers a vast specific surface area, while the small fraction of large-sized pores facilitates the mass transport of the electrolyte flow.

We also tested the electrochemical behaviour of our predicted optimal electrode microstructure by applying a homogeneous model. The result further verified that pursuing high SSA does not always promote better cell behaviour. Overly fined fibre can reduce the electrode velocity, weakening the transport process, which causes an insufficient electrochemical reaction and high overpotentials, increasing the non-reversible capacity.

Among the discussion of the optimization results, we also briefly discussed the calculation of the specific surface area using two different approaches, the sum of the voxel surface area and the Minkowski measures. Although it is not the main topic of this study, we believe it is essential to point out the inaccuracy of the voxel facets calculation.

As there is an ever-increasing demand for developing large-scale energy storage facilities, we are convinced that the computational optimization workflow presented in this study offers a practical methodology for future felt electrode design and paves the way for developing reliable redox flow batteries. We expect the industry to benefit from our findings and hope to report experimental results in the future.

5 <u>References</u>

1. Banerjee, R., Bevilacqua, N., Mohseninia, A., Wiedemann, B., Wilhelm, F., Scholta, J., and Zeis, R. (2019) Carbon felt electrodes for redox flow battery: Impact of compression on transport properties. *Journal of Energy Storage*, **26**, 100997.
2. Becker, J., Biebl, F., Glatt, E., Cheng, L., Grießer, A., Groß, M., Linden, S., Mosbach, D., Wagner, C., Weber, A., & Westerteiger, R. (2021) GeoDict (Release 2022).
3. Federer, H. (1996) Rectifiability BT - Geometric Measure Theory (eds.Federer, H., Eckmann, B., and van der Waerden, B.L.), Springer Berlin Heidelberg, Berlin, Heidelberg, pp. 207–340.
4. Sinha, P.K., Mukherjee, P.P., and Wang, C.Y. (2007) Impact of GDL structure and wettability on water management in polymer electrolyte fuel cells. *Journal of Materials Chemistry*, **17** (30), 3089–3103.
5. Qian, Y.H., D'Humières, D., and Lallemand, P. (1992) Lattice bgk models for navier-stokes equation. *Epl*, **17** (6), 479–484.
6. Kok, M.D.R., Jervis, R., Brett, D., Shearing, P.R., and Gostick, J.T. (2018) Insights into the Effect of Structural Heterogeneity in Carbonized Electrospun Fibrous Mats for Flow Battery Electrodes by X-Ray Tomography. *Small*, **14** (9), 1–15.
7. Hu, B., Luo, J., Hu, M., Yuan, B., and Liu, T.L. (2019) A pH-Neutral, Metal-Free Aqueous Organic Redox Flow Battery Employing an Ammonium Anthraquinone Anolyte. *Angewandte Chemie*, **131** (46), 16782–16789.
8. Patankar, S. (1980) *Numerical Heat Transfer and Fluid Flow*, CRC Press.
9. Latt, J., Malaspinas, O., Kontaxakis, D., Parmigiani, A., Lagrava, D., Brogi, F., Belgacem, M. Ben, Thorimbert, Y., Leclaire, S., Li, S., Marson, F., Lemus, J., Kotsalos, C., Conradin, R., Coreixas, C., Petkantchin, R., Raynaud, F., Beny, J., and Chopard, B. (2021) Palabos: Parallel Lattice Boltzmann Solver. *Computers & Mathematics with Applications*, **81**, 334–350.
10. Shodiev, A., Primo, E., Arcelus, O., Chouchane, M., Osenberg, M., Hilger, A., Manke, I., Li, J., and Franco, A.A. (2021) Insight on electrolyte infiltration of lithium ion battery electrodes by means of a new three-dimensional-resolved lattice Boltzmann model. *Energy Storage Materials*, **38** (February), 80–92.
11. Santos, J.E., Prodanović, M., Landry, C.J., and Jo, H. (2018) Determining the Impact of Mineralogy Composition for Multiphase Flow through Hydraulically Induced Fractures, in *Unconventional Resources Technology Conference, Houston, Texas, 23-25 July 2018*, pp. 2542–2556.
12. Ahrens, J., Geveci, B., and Law, C. (2005) ParaView: An End-User Tool for Large-Data Visualization. *The Visualization Handbook*.
13. van Rossum, G. (1995) Python tutorial, May 1995. *CWI Report CS-R9526*, (CS-R9526), 1–65.
14. Wan, S., Liang, X., Jiang, H., Sun, J., Djilali, N., and Zhao, T. (2021) A coupled machine learning and genetic algorithm approach to the design of porous electrodes for redox flow batteries. *Applied Energy*, **298**, 117177.
15. Shodiev, A., Zanotto, F.M., Yu, J., Chouchane, M., Li, J., and Franco, A.A. (2022) Designing Electrode Architectures to Facilitate Electrolyte Infiltration for Lithium-Ion Batteries. *Energy Storage Materials*, **49** (March), 268–277.
16. Zhang, D., Forner-Cuenca, A., Taiwo, O.O., Yufit, V., Brushett, F.R., Brandon, N.P., Gu, S., and Cai, Q. (2020) Understanding the role of the porous electrode microstructure in redox flow battery performance using an experimentally validated 3D pore-scale lattice Boltzmann model. *Journal of Power Sources*, **447** (August 2019), 227249.